Hong *et al. Microstructures* **2025**, *5*, 2025067
DOI: 10.20517/microstructures.2024.111

Microstructures

Review

Open Access

Check for updates

Solid-state nuclear magnetic resonance for garnet-type based solid lithium electrolytes

Geer Hong[1,#], Chenjie Lou[2,#], Mingxue Tang[1,2]

[1]College of Materials Science and Engineering & Key Laboratory of Advanced Materials and Devices for Post-Moore Chips, Ministry of Education, University of Science and Technology Beijing, Beijing 100083, China.
[2]Center for High Pressure Science and Technology Advanced Research, Beijing 100193, China.
[#]These authors contributed equally to this review.

Correspondence to: Dr. Chenjie Lou, Center for High Pressure Science and Technology Advanced Research, 10 Xibeiwang East Rd, Haidian District, Beijing 100193, China. E-mail: chenjielou@163.com; Prof. Mingxue Tang, College of Materials Science and Engineering, University of Science and Technology Beijing, 30, Xueyuan Road, Beijing 100083, China. E-mail: mxtang@ustb.edu.cn

How to cite this article: Hong, G.; Lou, C.; Tang, M. Solid-state nuclear magnetic resonance for garnet-type based solid lithium electrolytes. *Microstructures* **2025**, *5*, 2025067. https://dx.doi.org/10.20517/microstructures.2024.111

Received: 5 Nov 2024 **First Decision:** 20 Dec 2024 **Revised:** 11 Jan 2025 **Accepted:** 20 Feb 2025 **Published:** 12 Jun 2025

Academic Editor: Yida Deng **Copy Editor:** Shu-Yuan Duan **Production Editor:** Shu-Yuan Duan

Abstract

Solid-state batteries show high safety and theoretical energy density, receiving rapidly growing attention in both academic investigations and industrial applications. The garnet-type-based solid electrolytes (Garnet-SEs) play a vital role due to their high Li^+ conductivity and electrochemical stability. The atomic structure at local environments, such as the Li^+ coordination and site of doped ions, will have an important impact on the ability of transport and migration pathways that determine ion conductivity and electrochemical performances. In addition to the average structure from long-range perspective, the understanding at atomic level will be crucial for developing strategies to enhance ionic conductivity in Garnet-SEs. Solid-state NMR is a powerful tool that can probe the local atomic environments and dynamics on a molecular level. NMR is proven as a suitable technique for characterizing the light weight and small radius of Li elements, which is challenging for some conventional methods. In this review, atomic structure, ion pathways, and dynamic and microstructure formation of Garnet-SEs from the NMR view were discussed. These insights obtained from various NMR techniques will provide essential information for informing the control development and optimization of Garnet-SEs, contributing to the advancement of high-performance, safe, and reliable solid-state batteries.

Keywords: Solid electrolyte, nuclear magnetic resonance, local structure, lithium dynamic, migration pathway

© The Author(s) 2025. **Open Access** This article is licensed under a Creative Commons Attribution 4.0 International License (https://creativecommons.org/licenses/by/4.0/), which permits unrestricted use, sharing, adaptation, distribution and reproduction in any medium or format, for any purpose, even commercially, as long as you give appropriate credit to the original author(s) and the source, provide a link to the Creative Commons license, and indicate if changes were made.

INTRODUCTION

With the rapid growth in demand for mobile electronics, large-scale energy storage, *etc.*, exploring battery systems with high energy density and enhanced safety has become a key focus. Lithium-ion batteries (LIBs) are popular and widely used rechargeable batteries among various energy storage technologies. Solid-state batteries with solid electrolytes (SEs) can effectively achieve high energy density while improving safety. Since 1960s, several solid lithium-ion electrolytes have been reported, including Li-β-alumina[1], Li_3N[2], LISICON-type ($Li_{14}ZnGe_4O_{16}$, *etc.*)[3,4], NASICON-type [$Li_{1.3}Ti_{1.7}Al_{0.3}(PO_4)_3$, *etc.*][5], garnet-type [$Li_7La_3Zr_2O_{12}$ (LLZO), *etc.*][6], perovskite-type [$(Li, La)TiO_3$, *etc.*][7], LiPON-type [$Li_{2.88}PO_{3.86}N_{0.14}$, *etc.*][8], $Li_7P_3S_{11}$[9], argyrodite Li_6PS_5X (X = Cl, Br, I)[10] and thio-LISICON ($Li_{4-x}Ge_{1-x}P_xS_4$)[11], *etc.* Among these solid ion conductors, garnet-type electrolytes are the most sought-after, because of their high ionic conductivity, high chemical stability and wide electrochemical window[12,13].

The general structure of various oxide-based garnets is $A_3B_2C_3O_{12}$, which was first reported by Menzer in 1928[14]. Kasper reported the first lithium-based garnet-type solids $Li_3Ln_3M_2O_{12}$ (M = Te, W) in 1968[15], which were not further employed as SEs because of low ion conductivity. The first garnet-type lithium SE (Garnet-SEs) was claimed in 2003 by Werner Weppner, with the composition $Li_5La_3M_2O_{12}$ (M = Nb, Ta)[16]. Some Garnet-SEs were investigated by the replacement of La by alkaline earth ions in $Li_5La_3M_2O_{12}$, such as $Li_6ALa_2Ta_2O_{12}$ (A = Sr, Ba)[17], to achieve higher conductivity. Meanwhile, researchers reported Garnet-SEs by replacing M-ion by Bi^{5+}[18], Zr^{4+}[6], Te^{6+}[19], *etc.* Among these Garnet-SEs, Zr^{4+} replaced $Li_5La_3Ta_2O_{12}$ to form LLZO, offering the highest total conductivity. Figure 1 shows the molecular structures and corresponding ion conductivities of Garnet-SEs[20]. Investigation shows that pure LLZO is tetragonal (I41/acd) at room temperature (RT) with an ionic conductivity in an order of 10^{-6} S cm^{-1}, while the high-temperature cubic phase (Ia-3d) shows an ionic conductivity ranging from 10^{-4} to 10^{-3} S cm^{-1} at RT. The cubic phase can be easily obtained by super valent dopants Al^{3+}, which is likely from the ceramic crucible[21]. Ion doping was introduced to improve the conductivity, for example, doping ion at the Li sites (such as Al^{3+}[22-26], Ga^{3+}[27,28]), La site (such as Ce^{3+}[29,30]), Zr site (such as Ta^{5+}[31,32], Nb^{5+}[33], Te^{6+}[34]) and O site (such as F^-[35], Cl^-[36]) or co-doping in these sites[37-39]. Among them, the highest conductivity was achieved as 7.81×10^{-3} s cm^{-1} at 30 °C for Ga-doped LLZO[40,41].

However, the application of Garnet-SEs still faces many challenges, such as low ionic conductivity at RT, the formation of dendrites, *etc.* Improving room-temperature conductivity is a critical goal for practical battery applications. The growth of dendrites may destroy the interface between the electrolyte and the electrode, resulting in interface instability, which in turn affects the cycle life and safety of the battery. The formation of dendrites will lead to a short circuit phenomenon, which may cause thermal runaway in serious cases, affecting the safety and performance of the battery. Therefore, controlling dendrite growth is the key to improving the performance of garnet SEs.

Understanding the structure-activity relationship of ion conductivity is very important for the design and optimization of electrolytes. X-ray diffraction (XRD)[42] and neutron diffraction (ND)[43] methods provide average structural information from a long-range perspective. The ionic conductive behavior from electrochemical impedance spectroscopy (EIS)[44] mainly focuses on bulk materials and their interface. X-ray photoelectron spectroscopy (XPS)[45] can be used to characterize surface elements and their chemical states, and can disintegrate bulk phase information if combined with in-depth analysis, but it is limited in the detection of structural and dynamic information inside the material. However, the local structure plays a vital role for determining the ionic diffusion/transport and coordination stabilization, together with a significant influence on ion migration pathways. Therefore, it is crucial to probe the local structure, ion migration pathway, ion dynamic and microstructure formation in Garnet-SEs at the atomic scale for an

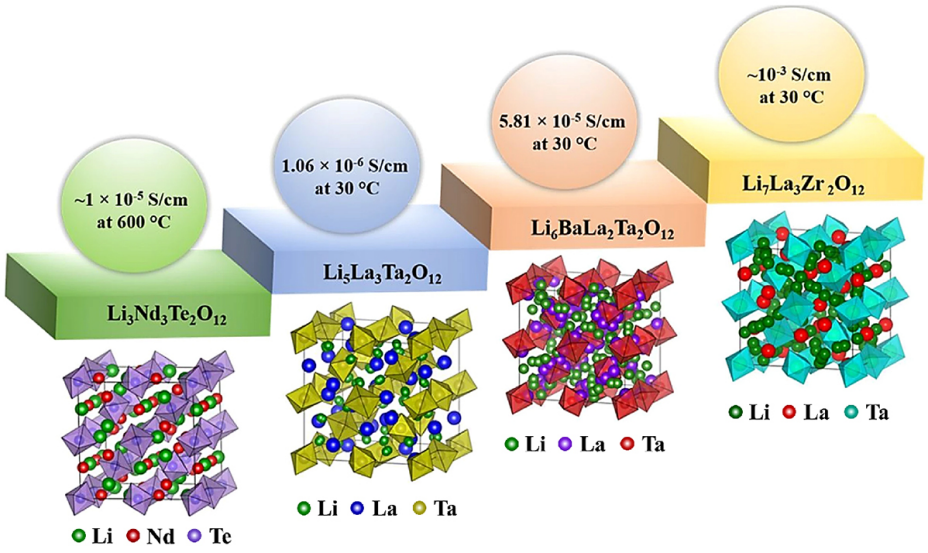

Figure 1. A schematic comparing the ionic conductivity and crystal structure of Garnet-SEs. Copyright 2021 Springer[20].

accurate understanding of the ion transport mechanism. A high-resolution transmission electron microscopy (TEM)[46] is a tool for the local structure, but it is not sensitive to light elements, such as Li atoms in the electrolytes. Instead, solid-state nuclear magnetic resonance (NMR) offers access to the investigation of local environments and dynamics on a molecular level[47-50], with the details about local symmetry, coordination numbers, and the dynamics of Li-ion mobility. The information provided by NMR can effectively analyze the local structure and dynamics of Garnet-SEs, with possible insights into the key limiting factors for lithium migration, which would, in turn, optimize Garnet-SEs design from an atomic or molecular view to improve their conductivity and stability. The NMR signal comes from the magnetic moment of atomic nuclei with a non-zero spin. When placed in a strong external magnetic field (B_0), these nuclear spins align either parallel or antiparallel to the field, creating a net magnetization moment along the B_0 direction. When a radiofrequency (RF) pulse, which equals the resonant frequency of the nuclei, is applied, the net magnetization moment is deflected so that it is no longer in the B_0 direction. When the RF pulse ends, the nuclear spins will precess around B_0, while the net magnetic moment deflects back to the B_0 direction. The precessing spins generate a detectable signal, the free induction decay (FID), which contains information about the local environment of the nuclei. The basic principle of NMR could be referred to our previous book chapter[51]. With the help of ultrafast-spinning, high field and different pulse techniques, such as cross-polarization (CP) under magic angle spinning (CPMAS), two-dimensional (2D) nuclear overhauser effect spectroscopy (NOESY), heteronuclear correlation (HETCOR), exchange spectroscopy (EXSY), rotary echo double resonance (REDOR), multiple-quantum magic-angle spinning (MQMAS) and temperature-dependent relaxation, *etc.*, the resolution of the spectra can be effectively improved for reliable component assignment, together with dynamics and migration behavior. Furthermore, NMR and imaging [magnetic resonance imaging (MRI)] with the aid of pulsed-field gradient (PFG) are non-deconstructive tools, which could be extended for *in-situ*/*in-operando* studies to track the evolution and lithium distribution inside electrolytes.

NMR technology covered in this review[52-54]

CP enhances the sensitivity of NMR experiments by transferring polarization from abundant, high-gyromagnetic ratio nuclei (typically ^{1}H and ^{19}F) to less abundant, low-gyromagnetic ratio nuclei of interest (e.g., ^{6}Li, ^{11}B, ^{15}N, ^{17}O, ^{27}Al, ^{71}Ga). This significantly improves the signal-to-noise ratio, especially for low-γ

nuclei often found in solid-state electrolytes (SEs).

MQMAS is a sophisticated technique used to overcome the effects of quadrupolar interactions, which are particularly problematic for nuclei with spin greater than 1/2 (e.g., ^{27}Al, ^{23}Na). It separates isotropic and anisotropic contributions to the NMR signal, resulting in higher resolution spectra, allowing for the identification of different sites and their environments within the SEs.

Double quantum (DQ)-single quantum (SQ) correlation spectroscopy is a powerful tool for studying the spatial proximity and connectivity of different nuclei in solids. By correlating DQ coherences with SQ coherences, DQ-SQ experiments provide information on internuclear distances and connectivities, offering insights into the local structure and ordering within the SEs.

Relaxation time (T_1 and T_2) provides information about the dynamic processes occurring within the SEs. The spin-lattice relaxation time (T_1) reflects the rate at which the nuclear spins return to thermal equilibrium after perturbation, while the spin-spin relaxation time (T_2) reflects the dephasing rate of the nuclear spins due to interactions with their surroundings. These measurements can provide insights into ion mobility, diffusion processes, and other dynamic phenomena crucial for understanding SEs' performance.

Spin-alignment echoes (SAE) refer to a phenomenon in which spins of nuclei become aligned due to interactions in a magnetic field. When a sample is subjected to a series of RF pulses, the spins can be manipulated to create a coherent state. After a certain time, these aligned spins can be refocused, leading to an echo signal that reflects the original alignment. This technique is useful for studying molecular dynamics and interactions within a sample.

Pulsed-gradient spin-echo (PGSE) is a technique used primarily in diffusion NMR to measure the diffusion of molecules in a medium. In PGSE, a pair of RF pulses is applied, separated by a time interval. During this interval, a magnetic field gradient is turned on and off. The gradient causes spins to dephase based on their position within the magnetic field, and when the second pulse is applied, the spins can be refocused. The degree of signal loss provides information about the diffusion properties of the molecules in the sample. This technique leverages the principles of magnetic resonance to extract valuable information about molecular dynamics and diffusion processes.

LOCAL STRUCTURE DETERMINATION

The atomic environment of Garnet-SEs and phase transformation were determined by the annealing process. Van Wüllen *et al.*[55] investigated the local structure of $Li_5La_3Nb_2O_{12}$ from NMR perspective, with the distribution of octahedrally-coordinated (Oct-Li) and tetrahedrally-coordinated Li (Tet-Li) cations sensitively depended on the annealing temperature. The electrolyte obtained at higher temperature (900 °C compared to 850 °C, called GR-900 and GR-850) displays higher concentrations of Oct-Li cations (84% than 60%) and higher lithium mobility, as shown in Figure 2A and B. The Oct-Li cations were considered as mobile species, whereas the Tet-Li cations seem to act as traps for Li cations. Nyman *et al.*[56] and Truong *et al.*[57] reported that decreasing the total Li^+ population in $Li_5La_3M_2O_{12}$ (M = Ta, Nb) electrolyte by taking advantage of the instability of lithium oxide or ion exchange for protons results in a decrease in the population of immobile Li^+ (Tet-Li cations) population, which is quantified by well-resolved[6,7] Li NMR spectra.

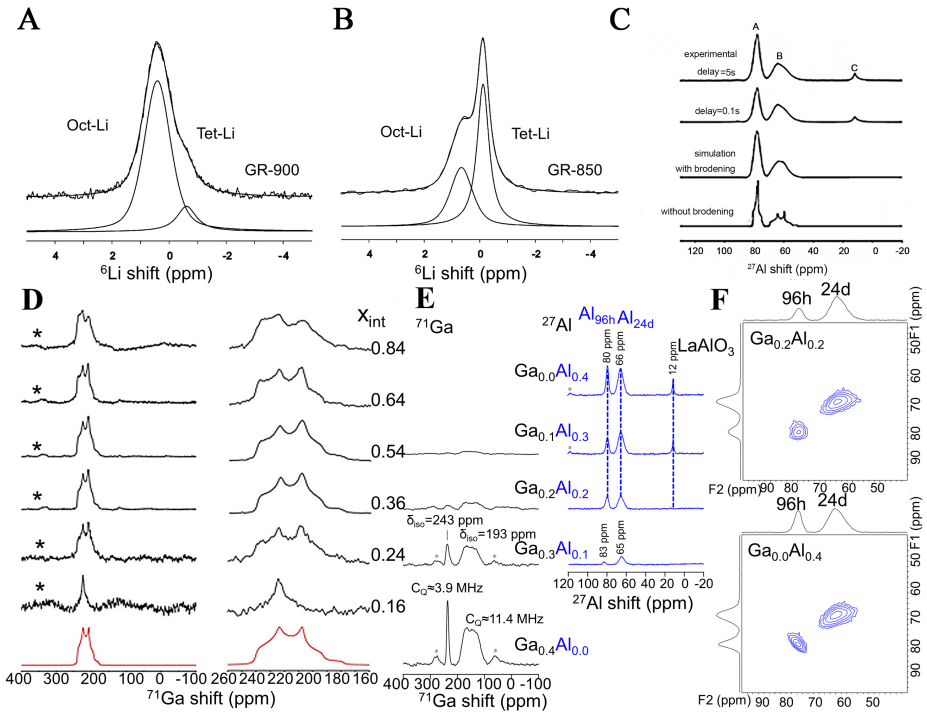

Figure 2. (A) ^{6}Li-MAS-NMR spectra for GR-900, taken at T = 200 K and; (B) GR-850, taken at room temperature. Copyright 2007, Royal Society of Chemistry[55]; (C) Experimental ^{27}Al MAS NMR spectra of cubic Al-containing LLZO at 14.1 T. Copyright 2011, American Chemical Society[21]; (D) ^{71}Ga MAS NMR spectra of Ga-doped LLZO. Copyright 2014, American Chemical Society[62]; (E) ^{71}Ga (black), ^{27}Al (blue) MAS NMR spectra and; (F) ^{27}Al 3QMAS NMR spectra of Al, Ga-doped LLZO recorded at 21.1 T. Copyright 2015, American Chemical Society[64]. MAS: Magic angle spinning; NMR: nuclear magnetic resonance; LLZO: $Li_7La_3Zr_2O_{12}$.

In the subsequent studies, Geiger *et al.*[21] found that the use of a ceramic crucible in initial synthesis steps introduces Al^{3+} into LLZO, which can obtain a stable cubic phase with higher ionic conductivity. Solid-state[27] ^{27}Al magic angle spinning (MAS) NMR in Figure 2C show the octahedrally-coordinated Al cations, being assigned to $LaAlO_3$, and two tetrahedrally-coordinated Al cations at 68 and 81 ppm. Besides, the content of $LaAlO_3$ will decrease after the sintering step, indicating that $LaAlO_3$ appears to be a precursor for the incorporation of Al into LLZO[58].

Manipulating Li ion sites and occupancy is vital to improve the conductivity of Garnet-SEs. Many works actively doped external elements into Garnet-SEs to regulate the occupancy of lithium. Kuhn *et al.*[59] and Düvel *et al.*[60] prepared cubic LLZO electrolytes with different Al contents. XRD and NMR results show that Al doping would form $LaAlO_3$, γ-$LiAlO_2$ and other Al environments in LLZO, indicating that Al atoms replaced Li, La, and Zr atoms. Rettenwander *et al.*[61] calculated ^{27}Al NMR chemical shifts using density functional theory and compared them to the experimental spectra, with the result showing that Al^{3+} prefers the regular (24d) and distorted (96h) tetrahedrally coordinated sites.

Rettenwander *et al.*[62] and Bernuy-Lopez *et al.*[63] prepared cubic Ga-bearing LLZO, and the ^{71}Ga NMR spectra plotted in Figure 2D show that Ga^{3+} mainly occurs in a distorted tetrahedrally coordinated site (96h). The site occupations of Ga and Al in garnets were probed with ^{27}Al and ^{71}Ga MAS NMR obtained from ultrahigh magnetic fields as well[64,65]. As shown in Figure 2E, ^{71}Ga MAS NMR spectra present two ^{71}Ga NMR resonances, corresponding to the 24d and 96h sites, respectively. The ^{27}Al signals can also be further assigned to the Al ions at the 24d and 96h sites, respectively. The second-order quadrupole interaction

always depresses the NMR spectral resolution, bringing difficulties for accurate assignments. The MQMAS technique was usually employed to improve spectral resolution for these materials with intensive quadrupole interaction. Figure 2F shows the ^{27}Al 3QMAS NMR spectra recorded at 21.1 T with two ^{27}Al environments, indicating that the line broadening is not caused by distinct overlapping sites.

Previous studies have generally assumed that the two resonances occurring in the ^{27}Al and ^{71}Ga NMR spectra correspond to the tetrahedrally coordinated 24d sites and distorted tetrahedrally coordinated 96h sites, respectively. Karasulu *et al.*[66] combined ^{17}O, ^{27}Al, and ^{71}Ga MAS NMR spectra and density-functional theory (DFT) calculations [Figure 3A-D]. In their opinion, both of the resonances observed in the ^{27}Al and ^{71}Ga NMR spectra are 24d (Li1) sites [rather than doping at other 96h (Li2) or La sites], resulting from deviations in the symmetry of the polyhedral coordination/site and changes in the number of occupied adjacent Li2 sites that share oxygen atoms with these dopant sites [Figure 3E]. The ^{17}O MAS spectra [Figure 3D] were used for the first time for the Garnet-SEs system, showing distinct and well-resolved resonances that are due to oxygen bound to the dopants (Al or Ga).

In the follow-up research, Vema *et al.*[67] demonstrated that Al and Ga dopants occupy only the 24d site in the LLZO lattice; the additional higher frequency resonance (~ 80 ppm for ^{27}Al and ~ 230 ppm for ^{71}Ga) in ^{27}Al and ^{71}Ga NMR spectra has been identified as being due to the side products, γ-$LiAlO_2$/$LiGaO_2$. As shown in Figure 4A and B, it can be seen that the signal of γ-$LiAlO_2$ matches the resonance in the LLZO sample well. The DQ-SQ spectrum of LLZO [Figure 4C] contains signals at ~ 10.5 ppm and ~ 79 ppm, indicating that these two sites are in Al-rich local environments, which can be assigned as $LaAlO_3$ and γ-$LiAlO_2$. The presence of these side-products can considerably affect the ionic conductivity of LLZO. The high-conductivity LLZO sample with a total conductivity of up to 1.75 mS cm^{-1} was prepared by adjusting the synthesis process.

Compared with doping elements, the sites and environment of lithium ions will directly determine the migration of lithium ions. Wang *et al.*[13] synthesized and investigated Te-doped LLZO with and without Al doping. The ^{6}Li NMR spectra show that the bulk conductivity of garnet-SEs is mainly determined by the mobility of Li ions at 24d sites. The resolution of the one-dimensional ^{7}Li or ^{6}Li spectra is still insufficient to resolve more specific Li sites in Garnet-SEs. Therefore, multiple dimensions or MQMAS NMR spectra were usually employed to gain deeper insights into the site assignment and correlation. Alternately, the saturation recovery method was used to probe the spinl-attice relaxation time (T_1) of Al and W co-doped Garnet-SEs[68], from which two different T_1 values, 1.0-5.0 s and 14-28 s, were obtained, respectively. The difference in T_1 was used to suppress the strong signals from the octahedral sites. The additional signal at 1.6 ppm was assigned as distorted octahedral sites (96h). With the help of this relaxation filter, 24d, 96h, and 48g sites can be well-resolved for the first time; the ^{6}Li MAS NMR spectra and simulation are shown in Figure 4D.

LI$^+$ MIGRATION PATHWAY PROBED BY NMR

Insight into ion migration pathways can enable researchers to target specific structural or compositional modifications that can enhance ionic conductivity and battery performance. Since Li$^+$ ions are light and small in radii, it is very challenging to experimentally probe their migration pathway by conventional methods, such as electron microscopy [transmission electron microscopy (TEM), scanning electron microscopy (SEM)]. Fortunately, NMR is isotope-specific and sensitive enough to detect the ^{6,7}Li signal. Therefore, EXSY NMR spectroscopy and element replacement from electrochemical cycling are popularly developed to unveil the Li transport pathway.

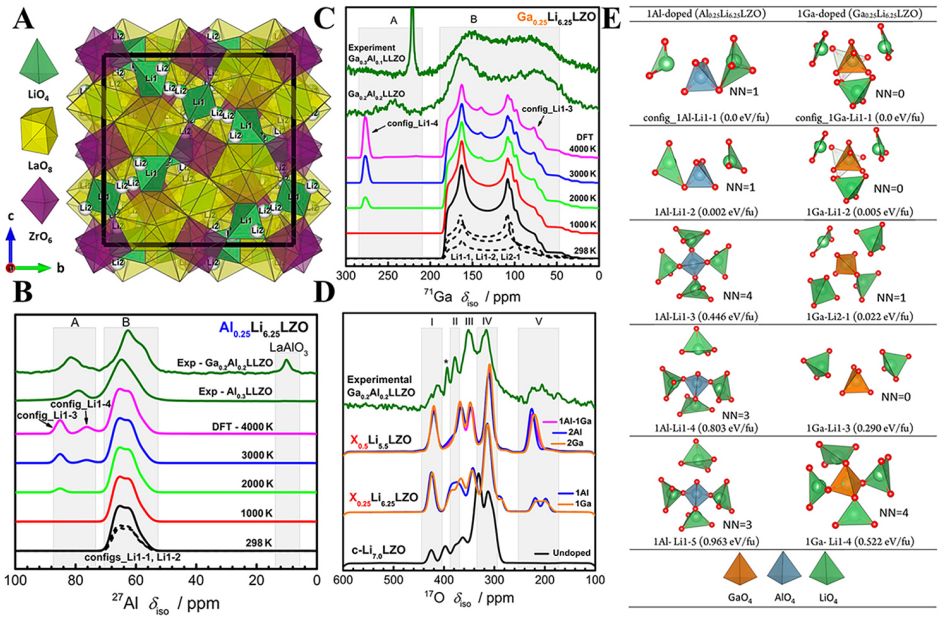

Figure 3. (A) Crystal structure of cubic-LLZO. DFT/GIPAW; (B) ^{27}Al and; (C) ^{71}Ga MAS NMR spectra of cubic $Al_{0.25}Li_{6.25}LZO$ models and cubic $Ga_{0.25}Li_{6.25}LZO$ models compared to the experimental spectrum of the $Ga_{0.2}Al_{0.2}LLZO$, $Al_{0.3}LLZO$ and $Ga_{0.3}Al_{0.1}LLZO$ samples; (D) DFT/GIPAW ^{17}O NMR spectra of cubic LLZO, $X_{0.25}Li_{6.25}LZO$ and $X_{0.5}Li_{5.5}LZO$ models compared to the experimental spectrum of the $Ga_{0.2}Al_{0.2}LLZO$ sample; (E) Local surroundings of the (left) Al and (right) Ga-doped sites in the selected single-doped defect configurations. Copyright 2020, American Chemical Society[66]. LLZO: $Li_7La_3Zr_2O_{12}$; DFT: density-functional theory; GIPAW: gauge-including projector augmented wave; NMR: nuclear magnetic resonance.

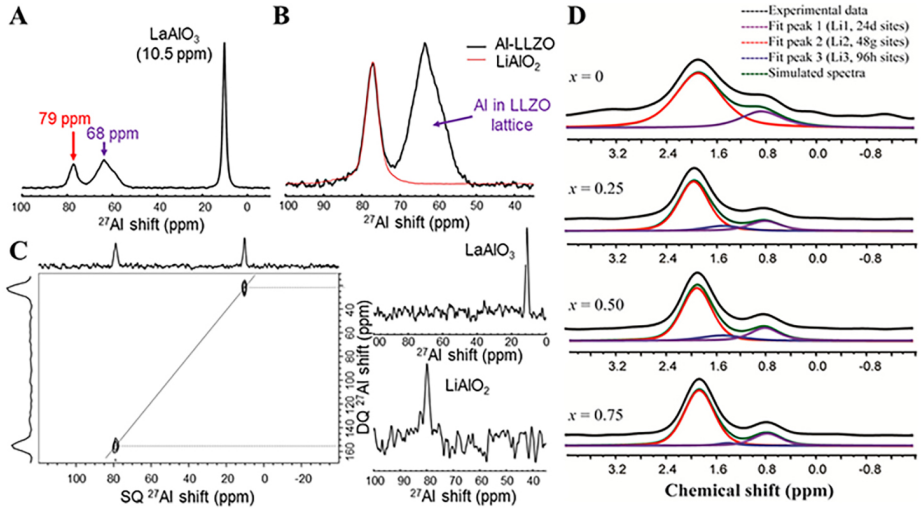

Figure 4. (A) ^{27}Al MAS NMR spectrum of the same Al-LLZO sample; (B) An enlargement of the same spectrum to show the resonances corresponding to Al in tetrahedral environments; (C) DQ-SQ 2D spectrum for the same Al-LLZO sample. Copyright 2023, American Chemical Society[67]; (D) ^{6}Li MAS NMR spectra of $Li_{7-2x-3y}Al_yLa_3Zr_{2-x}W_xO_{12}$ ($0 \le x \le 1$). Copyright 2015, American Chemical Society[68]. MAS: Magic angle spinning; NMR: nuclear magnetic resonance; LLZO: $Li_7La_3Zr_2O_{12}$; DQ: Double quantum; SQ: single quantum.

Wang *et al.*[68] applied the 2D ^{6}Li EXSY spectrum and found a cross-peak exists at the resonance of the 96h site (octahedral) and 24d site (tetrahedral) [Figure 5A], indicating that the Li^+ ions can jump between 24d and 96h sites, resulting in the total Li^+ pathway of 24d-96h-48g-96h-24d. Garnet-SEs are also introduced

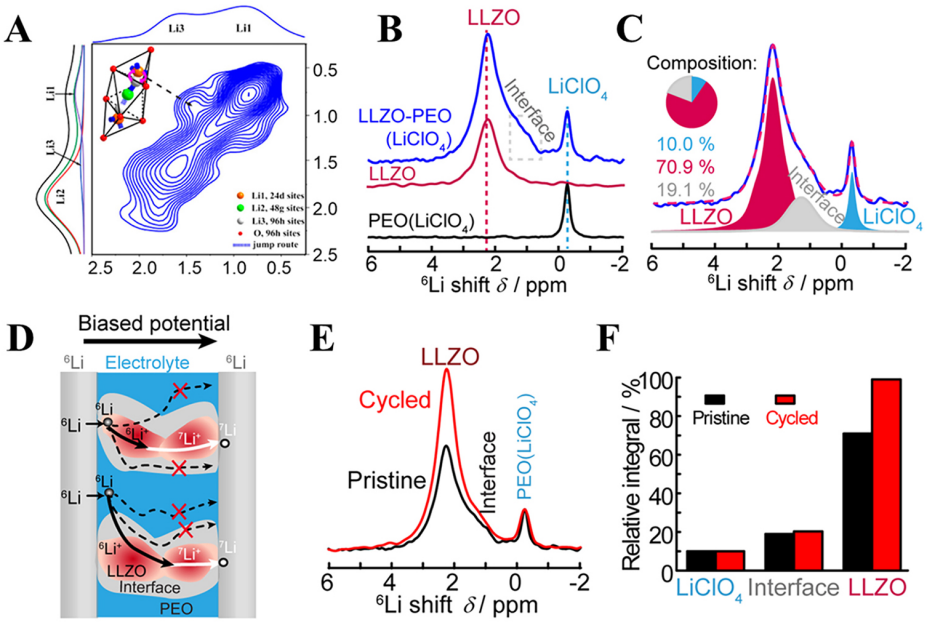

Figure 5. (A) ^{6}Li EXSY spectra of $Li_{7-2x-3y}Al_yLa_3Zr_{2-x}W_xO_{12}$ ($0 \leq x \leq 1$). Copyright 2015, American Chemical Society[68]; (B) ^{6}Li NMR of $LiClO_4$ in PEO, pure LLZO, and LLZO-PEO composite; (C) ^{6}Li CP NMR spectrum and quantification for the LLZO-PEO electrolyte; (D) Illustration of the symmetric ^{6}Li/composite electrolyte/^{6}Li battery and possible Li^+ transport pathways; (E) Comparison of the ^{6}Li NMR spectra of the LLZO-PEO composite electrolytes before (pristine) and after (cycled) cycling; (F) Quantitative analysis of ^{6}Li amount in $LiClO_4$, interface, and LLZO before and after cycling. Copyright 2016, Wiley-VCH[72]. EXSY: Exchange spectroscopy; LLZO: $Li_7La_3Zr_2O_{12}$; PEO: poly(ethylene oxide); NMR: nuclear magnetic resonance.

into polymers to yield composite electrolytes, which occupy the merits of the two with improved ionic conductivity and enhanced mechanical properties. Ranque *et al.*[69], Ghorbanzade *et al.*[70], and Ghorbanzade *et al.*[71] applied 2D ^{7}Li EXSY spectrum in the LLZO-poly(ethylene oxide) (PEO) system, showing an additional interface phase (such as LiOH) between the LLZO and PEO phases. The study reflected that the interface is involved in ion transport and has a positive effect.

Zheng *et al.*[72] creatively used isotope ion tracer exchange to determine the ion pathways in LLZO-PEO solid composite electrolyte. The signals of $LiClO_4$ in PEO, ceramic LLZO and interface can be clearly distinguished by highly resolved ^{6}Li NMR spectra in Figure 5B. The ^{1}H-^{6}Li CP NMR spectrum is plotted and quantified in Figure 5C, from which the LLZO takes up 71% and the concentration of interface is up to 19%. Figure 5D shows the symmetric battery, in which LLZO-PEO ($LiClO_4$) was used as an electrolyte and ^{6}Li metal was used as electrodes. ^{6}Li ions from the electrodes will replace ^{7}Li ions on their pathway inside the composite electrolyte during cycling. The ^{6}Li NMR difference between the pristine and the cycled composite electrolyte shows significantly increased and slightly increased intensity for the LLZO and interfacial Li, respectively. In contrast, the signal for the polymer $LiClO_4$ remains almost the same. The change in ^{6}Li signal indicates that Li ions tend to pass through the LLZO ceramic phase rather than the interface of a PEO-LLZO or PEO phase [Figure 5E and F]. Subsequently, this method has been adopted to many similar studies for the migration path determination[73,74]. Yang *et al.*[75] reported that Li^+ preferentially migrated within the LLZO/polymer interface in LLZO-PAN composite electrolyte. Zheng *et al.*[76] reported that Li ions are mainly transported via tetraethylene glycol dimethyl ether (TEGDME)-associated phases, not the LLZO or PEO when TEGDME is added to LLZO-PEO composite electrolyte as a small molecule additive. This method was also used by He *et al.*[77] to explore the influence of interfacial ion transport barriers in composite electrolytes under different current densities on the ion transport pathways. Wu et al.[78] showed

there is an extra high-speed Li-ion pathway between poly (vinyl ethylene carbonate) polymer phase and $Li_{6.75}La_3Zr_{1.75}Ta_{0.25}O_{12}$ by the aid of the formed chemical bonds and hydrogen bonds, resulting in high conductivity. Zhang *et al.*[79] conducted the Li-ion conduction mechanism of individual components within the LLZTO-PEO composite electrolyte, as shown in Figure 6. In organic-inorganic composite SE (OISE), polymer, LLZTO and Li-deficient layer three-phase synergistically promotes ion conduction, while lithium ions in OISE-L (the composite electrolyte containing Li_2CO_3 in LLZTO) are mainly conducted through the Li-deficient layer and the polymers, and Li_2CO_3 is involved in ionic conduction. Besides, at higher currents, lithium ions tend to pass through the polymer phase. In short, the isotope replacement from NMR perspective would offer a direct and reliable probe for the pathway of ion transport, which will in turn inform the design and optimization of ion conductors.

LI⁺ DYNAMICS FROM NMR

While ion transport properties in garnet-SEs are usually studied by EIS, NMR study will provide comprehensive time-domain dynamic information. Van Wüllen *et al.*[55] probed the dynamics of lithium ions in Garnet-SEs for the first time using temperature-dependent ^{7}Li NMR spectra in 2007, which was extended into a series of [80-82].

At low temperatures, the ^{7}Li NMR central line is Gaussian-like and broad due to the dipole-dipole interactions. The full width at half maximum (FWHM) at this temperature is wide (rigid lattice line width), and the jump rates of Li^+ are much smaller than 10^3 s^{-1}. As the temperature rises, the FWHM narrows due to the increasing averaged dipole-dipole interactions, which is called motional narrowing (MN), while line shape changes from Gaussian to Lorentzian. At high temperatures, dipole-dipole interactions are completely averaged due to sufficiently fast Li diffusion.

Narayanan *et al.* applied temperature-variable ^{7}Li NMR spectra of tetragonal LLZO, as shown in Figure 7A, showing typical MN. The empirical expression of Waugh and Fedin was used to obtain the activation energy (E_a), which is 0.47 eV, as given in

$$E_a^{WF} = 1.617 \times 10^{-3} \times \frac{T_{onset}}{K} \tag{1}$$

where T_{onset} denotes the onset temperature of MN[82].

The expression proposed by Abragam was also used to fit MN line (the dashed line in Figure 7A) and shows E_a = 0.43 eV, as given by

$$\delta(T) = \sqrt{\delta_0^2 \frac{2}{\pi} \arctan\left[\varsigma\delta(T)\tau_{0MN} \exp\left(\frac{E_a^{MN}}{k_B T}\right)\right] + \delta_\infty^2} \tag{2}$$

The diffusion-induced spin-lattice relaxation (SLR) NMR rate R_1 changes linearly with temperature, as follows:

$$R_{1(\rho)} \propto \begin{cases} \exp\left[\frac{E_{a\,low}}{k_B T}\right], & if\ T \gg T_{max} \\ \omega_{0(1)}^{\beta} \exp\left[-\frac{E_{a\,high}}{k_B T}\right], & if\ T \ll T_{max} \end{cases} \tag{3}$$

^{7}Li NMR SLR rates of LLZO [Figure 7B] were recorded and analyzed. The SLR rates reach their maximum at approximately T_{max} = 325 K and 530 K, respectively. The mean Li jump rates at these two temperatures can be calculated to be 1.9 × 10^5 s^{-1} and 4.9 × 10^8 s^{-1}, respectively. The self-diffusion coefficient D_{sd} can be obtained using the Einstein-Smoluchowski equation $D_{sd} = a^2/(6\tau)$ (3D diffusion), which is 1.3 × 10^{-17} m^2 s^{-1}

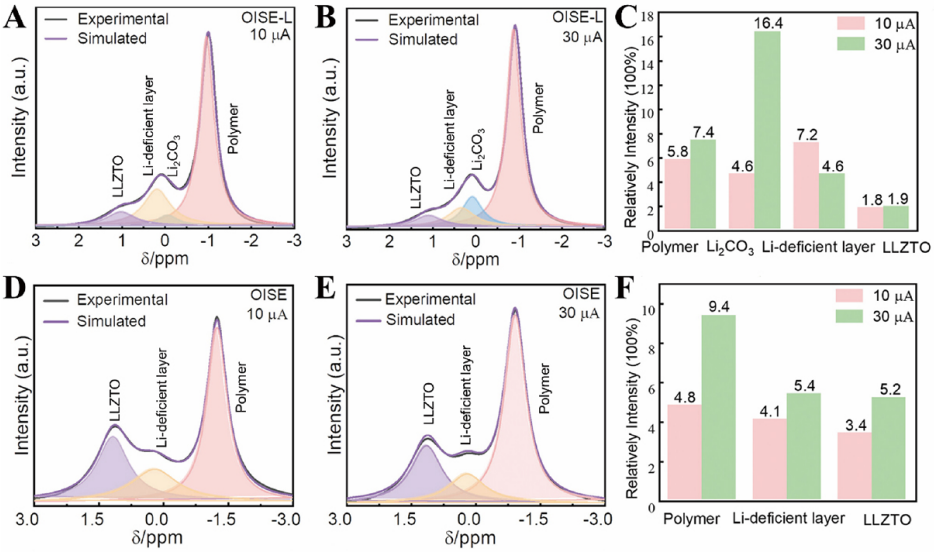

Figure 6. (A and B) ^{6}Li NMR spectra of OISE-L after ^{6}Li → ^{7}Li tracer exchange at 10 and 30 μA currents, respectively; (C) quantitative analysis of ^{6}Li amount in LLZTO, Li-deficient layer, Li_2CO_3 and $LiClO_4$ in PEO; (D and E) ^{6}Li NMR spectra of OISE after ^{6}Li → ^{7}Li tracer exchange at 10 and 30 μA currents, respectively; (F) quantitative analysis of ^{6}Li amount in LLZTO, Li-deficient layer, and $LiClO_4$ in PEO. Copyright 2024, Wiley-VCH[79]. NMR: nuclear magnetic resonance; OISE: Organic-inorganic composite solid-state electrolyte; PEO: poly(ethylene oxide).

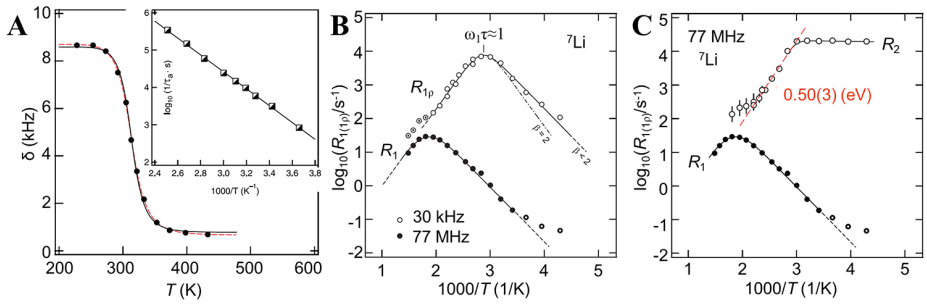

Figure 7. (A) ^{7}Li NMR line widths δ of the central line of tetragonal LLZO versus temperature. The dashed line represents a fit according to Equation (2) with no restrictions for the adjustable parameters. The solid line shows the same fit, however, with E_a being fixed at 0.5 eV. ^{7}Li NMR; (B) SLR rates and; (C) SSR rates of tetragonal LLZO recorded in both the laboratory (•) and the rotating frame of reference ( ). Copyright 2011, American Physical Society[82]. NMR: Nuclear magnetic resonance; LLZO: $Li_7La_3Zr_2O_{12}$; SLR: spin-lattice relaxation; SSR: spin-spin relaxation.

(325 K) and 3.3 × 10^{-14} m^2 s^{-1} (530 K).

As shown in Figure 7B, there is an asymmetric rate peak $R_{1\rho}$, showing the slope of the low-temperature flank (T < 330 K) is lower than that of the high-temperature flank, and leading to $E_{a\ low}$ = 0.32(3) eV < $E_{a\ high}$ = 0.48(3) eV. In general, only a small number of Li^+ jumps are sampled on the low-temperature flank of $R_{1\rho}$, indicating SLR was mainly caused by short-range Li motions in this temperature regime, while long-range Li diffusion is probed on the high-temperature flank. Meanwhile, spin-spin relaxation (SSR) NMR can also be used to extract the ion dynamic, and a similar E_a (0.50 eV) was obtained, as shown in Figure 7C.

To probe the Li^+ dynamics in different phases with various doped ions, Buschmann *et al.* and Bottke *et al.* applied ^{7}Li NMR spectroscopy to analyze Li-ion dynamics in Al-doped and Mo-doped cubic LLZO on

different range length scales[58,83]. The central transition and the satellite transitions of ^{7}Li NMR lines of Mo-doped LLZO are shown in Figure 8A. Figure 8B and C shows the line width of the central transition of Al-doped and Mo-doped LLZO, respectively. On the whole, the rigid lattice regime of cubic LLZO appears at lower temperatures, indicating higher Li^+ jump rate and fast Li-ion hopping processes than tetragonal LLZO [Figure 7A]. Interestingly, in contrast to Al-doped LLZO, the ^{7}Li NMR line shapes of Mo-doped LLZO undergo a relatively homogeneous MN. The smooth transition from the Gaussian shape to the Lorentz line at high temperatures suggests that most Li ions are involved in the diffusion process even at lower temperatures.

The rigid lattice line width of the central line and satellite intensity [Figure 8A] are 9 kHz and 150 kHz, respectively. At 273 K, the intensity of the satellite dropped drastically and completely evaporated at 446 K. At 396 K, the mean jump rate has already increased to the order faster than 10^6 s^{-1}. This indicates that averaging of quadrupole satellites occurs at relatively low temperatures, accompanied by the narrowing of the central line. This is sensitive to slow Li-ion diffusion, points to a subensemble of Li ions that are quite mobile on the time scale set by 150 kHz. All these indicate several diffusion processes are involved in Mo-doped LLZO.

^{7}Li NMR SLR rates (T_1^{-1}) are also investigated. The E_a of Al and Mo-doped LLZO acquired by R_1 is 0.12 and 0.15 eV [Figure 8D and E], respectively. These are lower than the E_a of pure tetragonal LLZO. However, the E_a is smaller than that obtained by EIS as expected since E_a from NMR relaxation is likely induced by short-range motions of the Li ions and possible unsuccessful Li jumps raised by correlation effects.

The broad shape of rate peak $T_{1\rho}^{-1}$ has been interpreted as a large distribution of jump rates and activation energies, resulting in the superposition of many SLR rate peaks at different temperatures. For Mo-doped LLZO, it can be well-reproduced with a combination of two individual rate peaks (dashed lines in Figure 8E), reflecting two possible different, fast ion diffusion processes in Mo-doped LLZO.

Other NMR techniques, such as stimulated echo correlation spectroscopy, could be developed to achieve E_a of SEs. Stimulated-echo experiments can powerfully analyze molecular dynamics with correlation times in the range of ms to s[80,84,85]. Via SAE NMR, it is likely to access long-range ion transport parameters with possible diffusion pathways. SAE was employed to probe the Li^+ dynamic in Mo-doped LLZO[83]. As shown in Figure 9, the ^{7}Li SAE NMR curves show there is one-step echo decay at low temperatures, and a second decay process gains in intensity at long mixing times with increasing temperatures. An E_a, $E_{a,SAE}$ = 0.29 eV, was deduced as shown in Figure 8E, which is in good agreement with those obtained by $T_{1\rho}$. The two-step delay of SAE NMR reveals heterogeneous dynamics, indicating that both 24d and 96h sites are involved in Li^+ diffusion. SAE decay curves recorded at long preparation times were also applied to accurately analyze dynamic processes, which shows a two-site jump process, with 96h-24d-96h' present in Mo-doped LLZO.

Since SEs are used mainly in micrometers or larger sizes for electrochemical devices, the migration in μm space can be provided with the help of the PGSE NMR method. Hayamizu *et al.*[86-91] applied the PGSE NMR method to measure the lithium-ion diffusion in Ta-doped LLZO. The observation time and PFG strength were varied to observe the lithium diffusion behavior, with lithium migration in Ta-doped LLZO distributed widely over a 10-100 ms timescale and a distance around 10^{-6} m. Wang *et al.*[68] obtained the diffusion coefficients of Al,W co-doped LLZO at different temperatures with the aid of PFG. The diffusion rates presented here are for those Li at the octahedral (48g) sites. Wang *et al.* probed the dynamics information of lithium-ion migration in LLZO and Al-doped LLZO[58-60,64,92,93], and Ga-doped LLZO[94] as well.

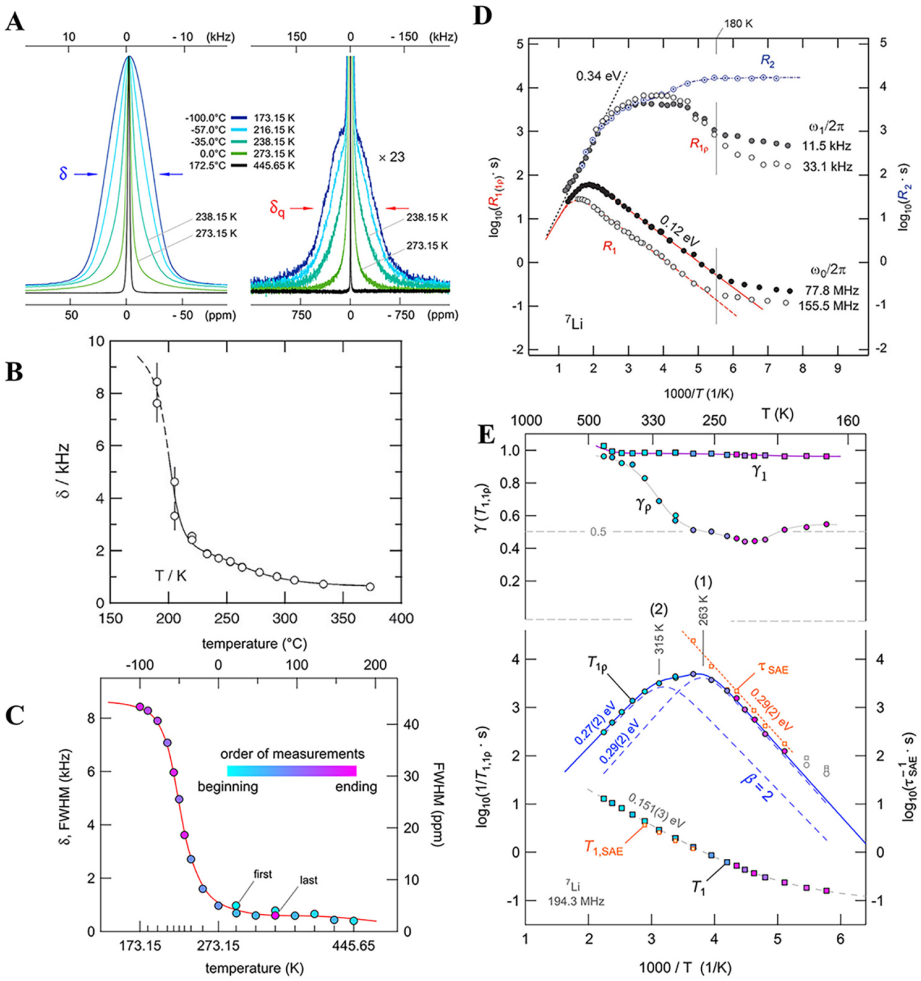

Figure 8. (A) Variable temperature ^{7}Li NMR spectra of Mo-doped LLZO. Copyright 2015, American Chemical Society[83]; The ^{7}Li NMR line width of the central transition (FWHM) of (B) Al-doped and; (C) Mo-doped LLZO as a function of temperature. Copyright 2011, Royal Society of Chemistry[58]. ^{6}Li NMR of $LiClO_4$ in PEO, pure LLZO, and LLZO-PEO composite; (D) Arrhenius plot of the ^{7}Li SLR NMR rates T_1^{-1} and $T_{1\rho}^{-1}$ of (D) Al-doped and; (E) Mo-doped LLZO. Copyright 2015, American Chemical Society[83]. NMR: Nuclear magnetic resonance; PEO: poly(ethylene oxide); LLZO: $Li_7La_3Zr_2O_{12}$; FWHM: full width at half maximum; PEO: poly(ethylene oxide); SLR: spin-lattice relaxation.

In short, NMR offers a wide range of techniques to investigate ion dynamics on different length scales and time scales in SEs[95-97], which has guiding implications for understanding the mechanism of ion migration within electrolytes and designing SEs with better performance. While T_1 relaxation times provide valuable information about local ion dynamics, they do not necessarily imply that these dynamics reflect the long-range transport behavior of charge carriers in operational cells.

DISTRIBUTION FROM MAGNETIC RESONANCE IMAGING

The growth of dendrites and the presence of dead lithium onto or inside SEs can seriously affect the life of solid-state batteries. The formation and growth of dendrites in garnet electrolytes are influenced by microstructure (i.e., SE density, grain size, *etc.*)[98], so it is important to map the dendrite distribution upon electrochemical cycling and feedback to the underlying origins. Various methods, such as DFT[99] and synchrotron X-ray tomography[100], have been used to study the microstructure formation in Garnet-SEs. Compared with these characterization methods, MRI shows the advantages of non-destructive monitoring

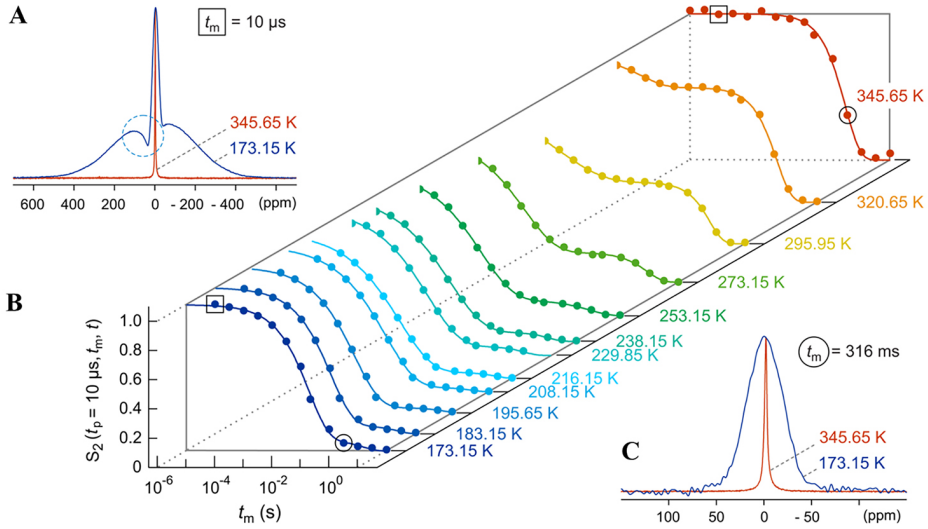

Figure 9. (A) Fourier transforms (173.15 and 345.65 K) of the ^{7}Li spin-alignment echoes of Mo-doped LLZO that were recorded at t_p = 10 μs and short t_m = 10 μs; (B) Stacked plot of the ^{7}Li NMR SAE single-spin (sin-sin) two-time correlation functions recorded at t_p = 10 μs. Copyright 2015, American Chemical Society[83]. LLZO: $Li_7La_3Zr_2O_{12}$; NMR: nuclear magnetic resonance; SAE: spin-alignment echoes.

and observation in real time. ^{7}Li MRI is widely used to detect the microstructural growth Li before observing visible symptoms in the voltage profiles during cycling. Marbella *et al.*[101] applied ^{7}Li NMR chemical shift imaging (CSI) to study the chemical and spatial information on Li microstructural growth in garnet-SEs. As shown in Figure 10A, LLZTO pellets with a diameter of ~ 5 mm and thickness of ~ 2.5 mm, and lithium metal disks in a diameter of 1.7 mm and thickness of 40 μm were used to assemble the symmetric battery. The ^{7}Li CSI of a pristine and short-circuit Li-LLZTO-Li cell are shown in Figure 10B and C, respectively. Due to the difference in chemical shift between LLZTO, lithium metal and lithium dendrites, their resonances can be well distinguished. LLZTO spans the length of the pellet, with lithium metal electrodes capping either side. The signal for Li microstructure varies according to the size and the direction relative to the magnetic field raised by the magnetic susceptibility effects[102]. Comparison of pristine, ^{7}Li CSI of short-circuited cells shows the emergence of a new signal at ~ 267 ppm, corresponding to microstructural Li. Besides, the presence of Li microstructure spans the entire electrolyte region caused by short-circuiting.

To probe the formation process of Li microstructures, cells were stopped at different galvanostatic cycling times; the discharge/charge (plating/stripping) profile and *ex-situ* analysis with ^{7}Li CSI of symmetric cells are shown in Figure 10D and E, respectively. Early during the cycling, the stable voltage plateaus and the CSIs which are similar to those of the pristine cell indicate almost no microstructural Li is formed. After one complete cycle, a slight sloping is observed in the voltage profile that coincides with the appearance of microstructural Li in the ^{7}Li CSI, indicating the Li microstructures are localized close to the electrode surface and are not yet detrimental to the cell. During charge at t_{cyc} = 480 min, soft shorts (voltage spikes) are observed, indicating that the microstructures are fine Li dendrites that fuse due to the melting lithium metal, which is consistent with the assignment of these voltage spikes. Finally, at t_{cyc} = 720 min, a sharp voltage drop is observed, which is consistent with the ^{7}Li resonance of microstructures that completely penetrates the SE and connects the two electrodes, indicating short-circuiting.

Chang *et al.*[103] combine NMR, MRI and *operando* acoustic techniques to study the effects of different stack pressures (SP) and galvanostatic charge currents on the microstructure formation at mesoscale and

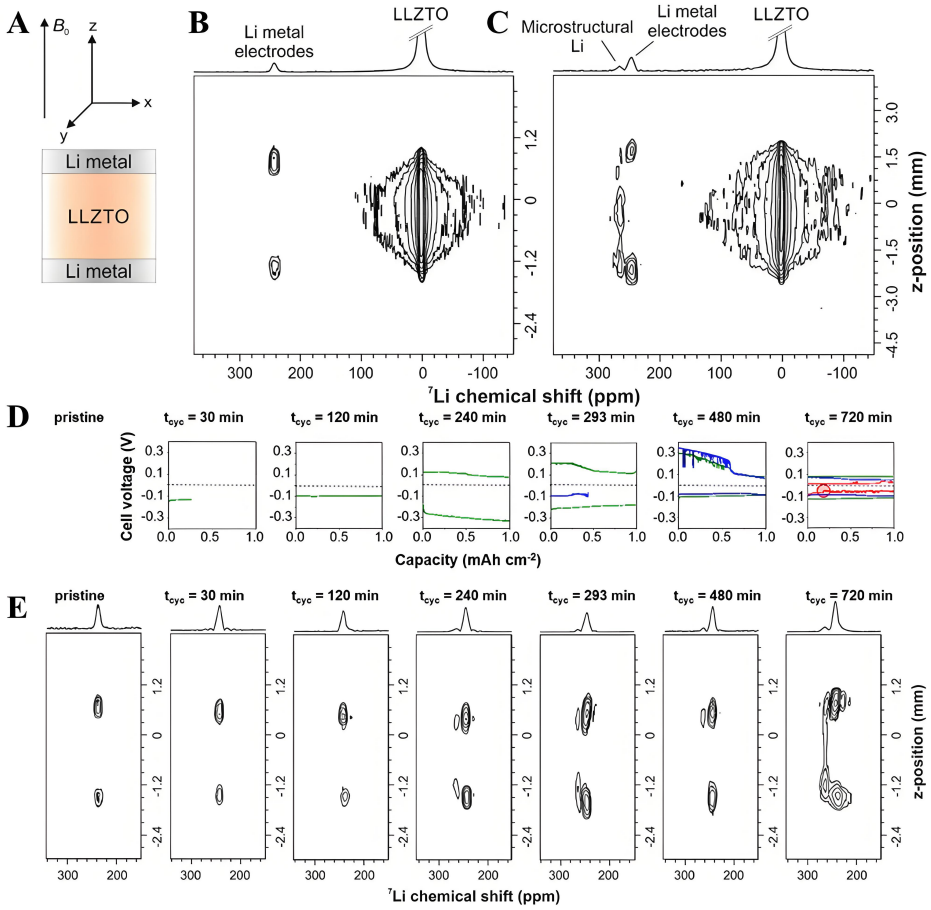

Figure 10. (A) Schematic of a symmetrical Li-LLZTO-Li cell depicting the orientation with respect to the external magnetic field, B_0, during the ^{7}Li CSI experiment; ^{7}Li chemical shift images of (B) pristine and; (C) cycled Li-LLZTO-Li symmetrical cells; (D) Galvanostatic cycling at 0.5 mA cm^{-2} for a maximum of 2 h per discharge/charge (plating/stripping) of Li-LLZTO-Li symmetrical cells stopped for *ex-situ* analysis with; (E) ^{7}Li CSI for pristine and different cycling time. Copyright 2019, American Chemical Society[101]. CSI: Chemical shift imaging.

microscopic scales as demonstrated in Figure 11. At 0.2 mA cm^{-2} or higher current, a SP of 2 MPa is insufficient to maintain the conformal interface between Li and LLZO. A SP of 7 MPa or higher can induce creep-driven interfacial dynamics, but it cannot eliminate the growth of microstructures indefinitely. A high SP of 13 MPa increases the local yield stress which leads to rupture and short circuit in the battery. Considering the inherent degradation patterns observed under high SPs and long durations of charge passed, low SP operation is required.

SUMMARY, CHALLENGE AND PROSPECT

In this review, we summarized the applications of solid-state NMR techniques in garnet-type-based SEs. It illustrates that NMR could access to determine the local atomic structure, ion pathway, ion dynamic and ion distribution of garnet-type SEs.

(1) The atomic structure is usually assigned by fundamental one-dimensional and advanced multiple dimensional NMR spectra, such as CPMAS, DQ-SQ spectra, and MQMAS, which can provide the proximity between homonuclei or improve the resolution of half-integer quadrupole nuclear spectra.

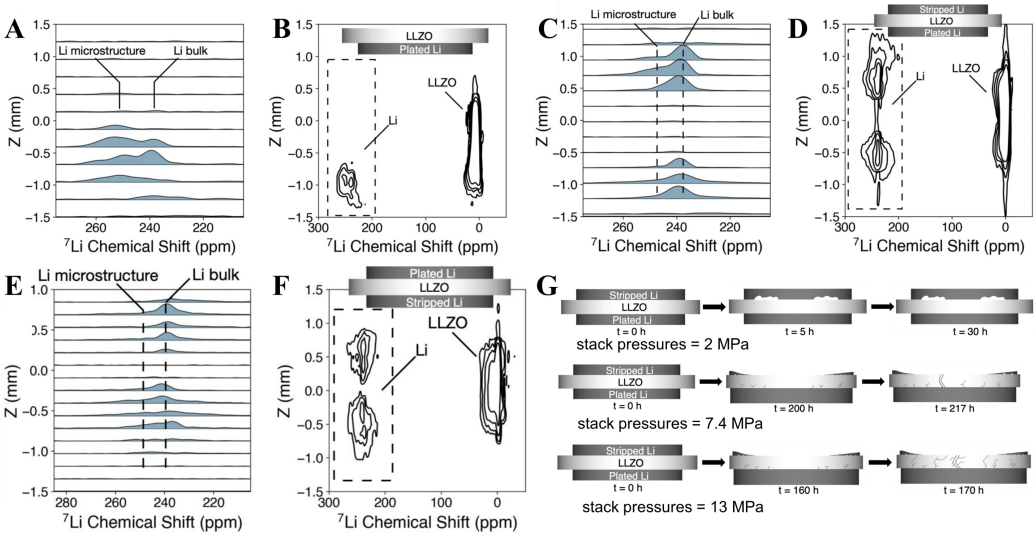

Figure 11. Lithium metal–LLZO interface at (A) and (B) 2 MPa. (A) 1D slices of the *ex-situ* ^{7}Li CSI experiment in the z-direction highlighting the lithium metal region between 200 and 280 ppm at (A) 2 MPa; (C) 7.4 MPa and; (E) 13 MPa, as indicated by the dashed region in (B), (D) and (E). Contour plot of *ex-situ* ^{7}Li CSI depicting a strong lithium metal resonance (~ 250 ppm) extending into the electrolyte region (0 ppm) in the z-direction at (B) 2 MPa; (D) 7.4 MPa and; (F) 13 MPa; (G) Simplified cartoon illustration of interface behavior. Copyright 2021, Springer Nature[103]. LLZO: $Li_7La_3Zr_2O_{12}$; CSI: chemical shift imaging.

(2) In addition, advanced techniques such as EXSY, isotope ion tracer exchange and variable temperature relaxation rates, SAE, and PGSE can determine the ion dynamics and migration pathway in SEs.

(3) Furthermore, MRI could track and map the formation and growth process of lithium microstructure, and the lithium evolution/distribution inside electrolytes upon electrochemical cycling. These obtained insights from NMR and MRI would help to understand atomic structure, dynamics and the limiting factors, which will, in turn, facilitate the design of SEs with enhanced performances.

However, several challenges hinder the widespread application of NMR in SEs.

(1) Traditional challenges. Sample preparation, cost and accessibility. Preparing suitable samples for solid-state NMR could be challenging, requiring careful consideration of factors such as particle size and packing density inside rotors, and external water and air need to be avoided at most of the time. High-field NMR spectrometers are expensive and require specialized expertise for operation and data analysis, limiting accessibility for many researchers.

(2) Low signal sensitivity. The inherently low sensitivity of NMR due to small Boltzmann distribution, together with the nuclei having large quadrupolar moments commonly used in SEs, requires long acquisition times and large sample quantities, which is impractical for scarce or expensive materials.

(3) Low spectral resolution. The rigid structure and anisotropic environments in SEs lead to broad NMR signals, reducing resolution and making spectral interpretation difficult, which will be exacerbated by the presence of paramagnetic impurities or defects. Complex SE compositions with multiple components can result in significant spectral overlap, complicating the assignment of individual signals and the quantification of different species.

(4) Interpretation of dynamic processes. Extracting quantitative information about ion transport mechanisms from NMR data can be challenging, requiring sophisticated experimental designs and data analysis techniques, which puts forward higher requirements for the measurement and data analysis of researchers.

(5) Design and assembly of battery cell. Battery cells used for solid-state NMR, especially *in-situ* solid-state NMR, require specialized cell designs that are non-magnetic and compatible with the NMR probe. These cells must allow for controlled electrochemical cycling while maintaining good NMR signal quality. This often involves compromises between electrochemical performance and NMR sensitivity, requiring careful optimization of cell design and materials[104,105].

Meanwhile, researchers need to take the following aspects into account.

(1) Develop forward-looking NMR techniques. Solid-state NMR suffers from low sensitivity due to small Boltzmann distribution. High magnetic field and cryoprobe at low temperatures can generate high Boltzmann distribution to improve the sensitivity. Ultrafast MAS for echoing signals from spinning sidebands to the isotropic resonances will also enhance sensitivity[106]. Dynamic nuclear polarization (DNP) can significantly increase sensitivity by transferring the high polarization of electrons to the nucleus under the condition of double resonance[107]. DNP has been applied to composite SEs[108]; Overhauser Effect DNP facilitates effective polarization transfer in the SEI for ^{6,7}Li isotopes *via* Li/Li$^+$ exchange as the key mechanism. Ultrafast MAS also can be used to enhance the resolution because it averages out the anisotropy of nuclei to narrow the signals. Temperature-dependent NMR spectra and relaxation can easily probe the dynamic in SEs[109], which depends on the development of high and low temperature probes. Additionally, 2D and 3D MRI and *in-situ* techniques can provide the distribution heterogeneity of specific elements in SEs; for example, ^{7}Li MRI reveals Li depletion from the electrode-electrolyte interfaces and increased heterogeneity of Li distribution upon electrochemical cycling[110].

(2) Expand the application of solid-state NMR to other systems to effectively study structural stability, interfacial reactions and products. Solid-state NMR is useful for probing the interfaces between electrodes and electrolytes, such as SE interphase (SEI) in solid batteries, which are critical for battery performance. Understanding the interfacial chemistry and stability can help in mitigating issues such as interfacial resistance and degradation. Additionally, solid-state NMR can help identify phase separation or segregation phenomena in composite materials or layered structures, which can affect the overall performance and stability of the battery. It can also monitor chemical reactions and degradation processes occurring during battery operation, providing insights into failure mechanisms and guiding the development of more stable materials. Furthermore, solid-state NMR can provide information about the mechanical properties of solid battery materials, helping to assess their brittleness, elasticity, and overall stability under operational conditions. The proposed NMR methods could also be adopted to other storage materials or systems, such as sodium-ion and lithium-air batteries.

With garnet-type SEs as the representative of SEs, this review summarizes what solid-state NMR technology can observe in solid batteries, which will enable researchers to have a more intuitive understanding of the role of solid-state NMR, and prospects of the challenges solid-state NMR faces in solid-state battery research and the future research directions, as shown in Table 1. In short, with the efforts of researchers, more cutting-edge NMR methods will be developed and applied to solve key problems in solid-state batteries for achieving higher performances.

Table 1. Features to be measured connected to NMR methods and limits and future pathways

Features	Specific features	NMR methods	Limits	Future pathways
Local structure	Composition, atom/ion site, internuclear distance	1D spectrum, MQMAS, REDOR, NOESY, HETCOR	Low resolution, requires specialized expertise for data analysis	Higher magnetic field and ultrafast MAS, software that is easier to use
Interface	SEI, Decomposition product	CP, DNP, *In-situ* NMR	The high cost of DNP and *in-situ* NMR, small sample, require specialized expertise for operation and data analysis	Methods for increasing sensitivity
Pathway of ion	Ion transport pathway and direction	EXSY, SAE	Requires a wide range of temperature variations for SAE	Ultra-low/high temperature probe
Ion dynamic	Diffusion mode and dimension, diffusion coefficient, activation energy	T_1, T_2 (VT), SAE, PGSE, PFG NMR	Requires a wide range of temperature variations, and requires specialized expertise for operation and data analysis	Ultra-low/high temperature MAS probe
Formation of microstructures	Dendrite growth, element distribution, structure and morphology evolution	CSI, MRI, *In-situ* NMR	High cost, low resolution, design and assembly of battery cells, requires specialized expertise for operation and data analysis	Develop new sequences and techniques to simplify operations and improve resolution

MQMAS: Multiple-quantum magic-angle spinning; REDOR: rotary echo double resonance; NOESY: nuclear overhauser effect spectroscopy; HETCOR: heteronuclear correlation; CP: cross-polarization; DNP: dynamic nuclear polarization NMR: nuclear magnetic resonance; EXSY: exchange spectroscopy; SAE: spin-alignment echoes; PGSE: pulsed-gradient spin-echo; PFG: pulsed-field gradient; CSI: chemical shift imaging; MRI: magnetic resonance imaging.

DECLARATIONS

Acknowledgments
The platform of HPSTAR is acknowledged.

Authors' contributions
Characterization, original draft writing: Lou, C.; Hong, G.
Review, editing and supervision: Tang, M.; Lou, C.

Availability of data and materials
Not applicable.

Financial support and sponsorship
This work was supported by the National Natural Science Foundation of China (Grant 22090043) and China Postdoctoral Science Foundation projects (Grant 2024M761644).

Conflicts of interest
All authors declared that there are no conflicts of interest.

Ethical approval and consent to participate
Not applicable.

Consent for publication
Not applicable.

Copyright
© The Author(s) 2025.

REFERENCES

1. Yu, Y.; Kummer, J. Ion exchange properties of and rates of ionic diffusion in beta-alumina. *J. Inorg. Nucl. Chem.* **1967**, *29*, 2453-75. DOI
2. Alpen, U. V.; Rabenau, A.; Talat, G. H. Ionic conductivity in Li_3N single crystals. *Appl. Phys. Lett.* **1977**, *30*, 621-3. DOI
3. Hong, H. Crystal structure and ionic conductivity of $Li_{14}Zn(GeO_4)_4$ and other new Li^+ superionic conductors. *Mater. Res. Bull.* **1978**, *13*, 117-24. DOI
4. Alpen, U.; Bell, M.; Wichelhaus, W.; Cheung, K.; Dudley, G. Ionic conductivity of $Li_{14}Zn(GeO_{44}$ (Lisicon). *Electrochimica. Acta.* **1978**, *23*, 1395-7. DOI
5. Aono, H.; Imanaka, N.; Adachi, G. High Li^+ conducting ceramics. *Acc. Chem. Res.* **1994**, *27*, 265-70. DOI
6. Murugan, R.; Thangadurai, V.; Weppner, W. Fast lithium ion conduction in garnet-type $Li_7La_3Zr_2O_{12}$. *Angew. Chem. Int. Ed. Engl.* **2007**, *46*, 7778-81. DOI PubMed
7. Inaguma, Y.; Liquan, C.; Itoh, M.; et al. High ionic conductivity in lithium lanthanum titanate. *Solid. State. Communications.* **1993**, *86*, 689-93. DOI
8. Wang, B.; Chakoumakos, B.; Sales, B.; Kwak, B.; Bates, J. Synthesis, crystal structure, and ionic conductivity of a polycrystalline lithium phosphorus oxynitride with the γ-Li_3PO_4 structure. *J. Solid. State. Chem.* **1995**, *115*, 313-23. DOI
9. Mizuno, F.; Hayashi, A.; Tadanaga, K.; Tatsumisago, M. High lithium ion conducting glass-ceramics in the system Li_2S-P_2S_5. *Solid. State. Ionics.* **2006**, *177*, 2721-5. DOI
10. Kato, Y.; Hori, S.; Saito, T.; et al. High-power all-solid-state batteries using sulfide superionic conductors. *Nat. Energy.* **2016**, *1*, 16030. DOI
11. Kanno, R.; Murayama, M. Lithium ionic conductor thio-LISICON: The Li_2S-GeS_2-P_2S_5 system. *J. Electrochem. Soc.* **2001**, *148*, A742. DOI
12. Luo, W.; Gong, Y.; Zhu, Y.; et al. Reducing interfacial resistance between garnet-structured solid-state electrolyte and li-metal anode by a germanium layer. *Adv. Mater.* **2017**, 29. DOI
13. Wang, D.; Zhong, G.; Dolotko, O.; et al. The synergistic effects of Al and Te on the structure and Li^+-mobility of garnet-type solid electrolytes. *J. Mater. Chem. A.* **2014**, *2*, 20271-9. DOI
14. Menzer, G. XX. Die Kristallstruktur der Granate. *Z. Kristallogr. Cryst. Mater.* **1929**, *69*, 300-96. DOI
15. Kasper, H. M. Series of rare earth garnets $Ln^{3+}{}_3M_2Li^+{}_3O_{12}$ (M = Te, W). *Inorg. Chem.* **1969**, *8*, 1000-2. DOI
16. Thangadurai, V.; Kaack, H.; Weppner, W. J. F. Novel fast Lithium ion conduction in garnet-type $Li_5La_3M_2O_{12}$ (M = Nb, Ta). *J. Am. Ceram. Soc.* **2003**, *86*, 437-40. DOI
17. Thangadurai, V.; Weppner, W. Li_6 $ALa_2Ta_2O_{12}$ (A = Sr, Ba): novel garnet-like oxides for fast lithium ion conduction. *Adv. Funct. Mater.* **2005**, *15*, 107-12. DOI
18. Murugan, R.; Weppner, W.; Schmid-beurmann, P.; Thangadurai, V. Structure and lithium ion conductivity of bismuth containing lithium garnets $Li_5La_3Bi_2O_{12}$ and $Li_6SrLa_2Bi_2O_{12}$. *Mater. Sci. Eng:. B.* **2007**, *143*, 14-20. DOI
19. O'callaghan, M. P.; Lynham, D. R.; Cussen, E. J.; Chen, G. Z. Structure and ionic-transport properties of lithium-containing garnets $Li_3Ln_3Te_2O_{12}$ (Ln = Y, Pr, Nd, Sm-Lu). *Chem. Mater.* **2006**, *18*, 4681-9. DOI
20. Alexander, G. V.; S, I. M.; Murugan, R. Review on the critical issues for the realization of all-solid-state lithium metal batteries with garnet electrolyte: interfacial chemistry, dendrite growth, and critical current densities. *Ionics* **2021**, *27*, 4105-26. DOI
21. Geiger, C. A.; Alekseev, E.; Lazic, B.; et al. Crystal chemistry and stability of "$Li_7La_3Zr_2O_{12}$" garnet: a fast lithium-ion conductor. *Inorg. Chem.* **2011**, *50*, 1089-97. DOI
22. Li, Y.; Han, J. T.; Wang, C. A.; et al. Ionic distribution and conductivity in lithium garnet $Li_7La_3Zr_2O_{12}$. *J. Power. Sources.* **2012**, *209*, 278-81. DOI
23. Jin, Y.; Mcginn, P. J. Al-doped $Li_7La_3Zr_2O_{12}$ synthesized by a polymerized complex method. *J. Power. Sources.* **2011**, *196*, 8683-7. DOI
24. Rangasamy, E.; Wolfenstine, J.; Sakamoto, J. The role of Al and Li concentration on the formation of cubic garnet solid electrolyte of nominal composition $Li_7La_3Zr_2O_{12}$. *Solid. State. Ionics.* **2012**, *206*, 28-32. DOI
25. El-shinawi, H.; Paterson, G. W.; Maclaren, D. A.; Cussen, E. J.; Corr, S. A. Low-temperature densification of Al-doped $Li_7La_3Zr_2O_{12}$: a reliable and controllable synthesis of fast-ion conducting garnets. *J. Mater. Chem. A.* **2017**, *5*, 319-29. DOI
26. Rosenkiewitz, N.; Schuhmacher, J.; Bockmeyer, M.; Deubener, J. Nitrogen-free sol-gel synthesis of Al-substituted cubic garnet $Li_7La_3Zr_2O_{12}$ (LLZO). *J. Power. Sources.* **2015**, *278*, 104-8. DOI
27. Qin, S.; Zhu, X.; Jiang, Y.; Ling, M.; Hu, Z.; Zhu, J. Growth of self-textured Ga^{3+}-substituted $Li_7La_3Zr_2O_{12}$ ceramics by solid state reaction and their significant enhancement in ionic conductivity. *Appl. Phys. Lett.* **2018**, *112*, 113901. DOI
28. Wu, J. F.; Chen, E. Y.; Yu, Y.; et al. Gallium-Doped $Li_7La_3Zr_2O_{12}$ Garnet-type electrolytes with high lithium-ion conductivity. *ACS. Appl. Mater. Interfaces.* **2017**, *9*, 1542-52. DOI
29. Dong, B.; Yeandel, S. R.; Goddard, P.; Slater, P. R. Combined experimental and computational study of Ce-doped $La_3Zr_2Li_7O_{12}$ garnet solid-state electrolyte. *Chem. Mater.* **2020**, *32*, 215-23. DOI
30. Rangasamy, E.; Wolfenstine, J.; Allen, J.; Sakamoto, J. The effect of 24c-site (A) cation substitution on the tetragonal-cubic phase transition in $Li_{7-x}La_{3-x}A_xZr_2O_{12}$ garnet-based ceramic electrolyte. *J. Power. Sources.* **2013**, *230*, 261-6. DOI
31. Thompson, T.; Wolfenstine, J.; Allen, J. L.; et al. Tetragonal vs. cubic phase stability in Al - free Ta doped $Li_7La_3Zr_2O_{12}$ (LLZO). *J.*

Mater. Chem. A. **2014**, *2*, 13431-6. DOI

32. Zhou, Y.; Li, X.; Yang, Y.; Huang, X.; Tian, B. Production of Ta-doped $Li_7La_3Zr_2O_{12}$ solid electrolyte with high critical current density. *ACS. Appl. Energy. Mater.* **2022**, *5*, 13817-28. DOI
33. Ohta, S.; Kobayashi, T.; Asaoka, T. High lithium ionic conductivity in the garnet-type oxide $Li_{7-x}La_3(Zr_{2-x}, Nb_x)O_{12}$ (x = 0-2). *J. Power. Sources.* **2011**, *196*, 3342-5. DOI
34. Deviannapoorani, C.; Dhivya, L.; Ramakumar, S.; Murugan, R. Lithium ion transport properties of high conductive tellurium substituted $Li_7La_3Zr_2O_{12}$ cubic lithium garnets. *J. Power. Sources.* **2013**, *240*, 18-25. DOI
35. Shi, J.; Sun, G.; Li, L.; et al. Fluorine substitution at the O-site imparts enhanced chemical stability for garnet-structured electrolytes. *ACS. Energy. Lett.* **2023**, *8*, 48-55. DOI
36. Wang, S.; Zeng, T.; Wen, X.; et al. Optimized lithium ion coordination via chlorine substitution to enhance ionic conductivity of garnet-based solid electrolytes. *Small* **2024**, *20*, e2309874. DOI
37. Sun, F.; Yang, Y.; Zhao, S.; et al. Local Li^+ framework regulation of a garnet-type solid-state electrolyte. *ACS. Energy. Lett.* **2022**, *7*, 2835-44. DOI
38. Miara, L. J.; Ong, S. P.; Mo, Y.; et al. Effect of Rb and Ta doping on the ionic conductivity and stability of the garnet $Li_{7+2x-y}(La_{3-x}Rb_x)(Zr_{2-y}Ta_y)O_{12}$ ($0 \le x \le 0.375$, $0 \le y \le 1$) superionic conductor: a first principles investigation. *Chem. Mater.* **2013**, *25*, 3048-55. DOI
39. Ma, K.; Chen, B.; Li, C.; Thangadurai, V. Experimental and computational study of Mg and Ta-doped $Li_7La_3Zr_2O_{12}$ garnet-type solid electrolytes for all-solid-state lithium batteries. *Adv. Sustain. Syst.* **2024**, *8*, 2300656. DOI
40. Sharifi, O.; Golmohammad, M.; Soozandeh, M.; Mehranjani, A. S. Improved Ga-doped $Li_7La_3Zr_2O_{12}$ garnet-type solid electrolytes for solid-state Li-ion batteries. *J. Solid. State. Electrochem.* **2023**, *27*, 2433-44. DOI
41. Wang, Y.; Chen, Z.; Jiang, K.; Shen, Z.; Passerini, S.; Chen, M. Accelerating the development of LLZO in Solid-state batteries toward commercialization: a comprehensive review. *Small* **2024**, *20*, e2402035. DOI
42. Kuhn, A.; Köhler, J.; Lotsch, B. V. Single-crystal X-ray structure analysis of the superionic conductor $Li_{10}GeP_2S_{12}$. *Phys. Chem. Chem. Phys.* **2013**, *15*, 11620-2. DOI PubMed
43. Arbi, K.; Hoelzel, M.; Kuhn, A.; García-Alvarado, F.; Sanz, J. Local structure and lithium mobility in intercalated $Li_3Al_xTi_{2-x}(PO_4)_3$ NASICON type materials: a combined neutron diffraction and NMR study. *Phys. Chem. Chem. Phys.* **2014**, *16*, 18397-405. DOI
44. Arbi, K.; Bucheli, W.; Jiménez, R.; Sanz, J. High lithium ion conducting solid electrolytes based on NASICON $Li_{1+x}Al_xM_{2-x}(PO_4)_3$ materials (M = Ti, Ge and $0 \le x \le 0.5$). *J. Eur. Ceram. Soc.* **2015**, *35*, 1477-84. DOI
45. Zhou, Y.; Gao, A.; Duan, M.; et al. Quasi-in situ XPS insights into the surface chemistry of garnet-type $Li_{6.4}La_3Zr_{1.4}Ta_{0.6}O_{12}$ solid-state electrolytes: the overlooked impact of pretreatments and a direct observation of the formation of LiOH. *ACS. Appl. Mater. Interfaces.* **2023**, *15*, 45465-74. DOI
46. Gao, X.; Fisher, C. A. J.; Ikuhara, Y. H.; et al. Cation ordering in A-site-deficient Li-ion conducting perovskites $La_{(1-x)/3}Li_xNbO_3$. *J. Mater. Chem. A.* **2015**, *3*, 3351-9. DOI
47. Lou, C.; Liu, J.; Sun, X.; et al. Correlating local structure and migration dynamics in Na/Li dual ion conductor $Na_5YSi_4O_{12}$. *Proc. Natl. Acad. Sci. U. S. A.* **2024**, *121*, e2401109121. DOI PubMed PMC
48. Sun, G.; Lou, C.; Yi, B.; et al. Electrochemically induced crystalline-to-amorphization transformation in sodium samarium silicate solid electrolyte for long-lasting sodium metal batteries. *Nat. Commun.* **2023**, *14*, 6501. DOI PubMed PMC
49. Lou, C.; Zhang, W.; Liu, J.; et al. The glass phase in the grain boundary of $Na_3Zr_2Si_2PO_{12}$, created by gallium modulation. *Chem. Sci.* **2024**, *15*, 3988-95. DOI
50. Shi, Y.; Fu, J.; Hui, K.; et al. Promoting the electrochemical properties of yolk-shell-structured CeO_2 composites for lithium-ion batteries. *Microstructures* **2021**, *1*, 2021005. DOI
51. Shen, C. Microscopy and Microanalysis for Lithium-Ion Batteries. 1st ed. CRC Press; 2023. DOI
52. Reif, B.; Ashbrook, S. E.; Emsley, L.; Hong, M. Solid-state NMR spectroscopy. *Nat. Rev. Methods. Primers.* **2021**, *1*, 2. DOI PubMed PMC
53. Chien, P.; Griffith, K. J.; Liu, H.; Gan, Z.; Hu, Y. Recent advances in solid-state nuclear magnetic resonance techniques for materials research. *Annu. Rev. Mater. Res.* **2020**, *50*, 493-520. DOI
54. Brown, S. P.; Spiess, H. W. Advanced solid-state NMR methods for the elucidation of structure and dynamics of molecular, macromolecular, and supramolecular systems. *Chem. Rev.* **2001**, *101*, 4125-56. DOI PubMed
55. Wüllen L, Echelmeyer T, Meyer HW, Wilmer D. The mechanism of Li-ion transport in the garnet $Li_5La_3Nb_2O_{12}$. *Phys. Chem. Chem. Phys.* **2007**, *9*, 3298-303. DOI PubMed
56. Nyman, M.; Alam, T. M.; Mcintyre, S. K.; Bleier, G. C.; Ingersoll, D. Alternative approach to increasing Li mobility in Li-La-Nb/Ta garnet electrolytes. *Chem. Mater.* **2010**, *22*, 5401-10. DOI
57. Truong, L.; Thangadurai, V. Soft-Chemistry of Garnet-Type $Li_{5+x}Ba_xLa_{3-x}Nb_2O_1$ (x = 0, 0.5, 1): Reversible $H^+ \leftrightarrow Li^+$ ion-exchange reaction and their X-ray, ^{7}Li MAS NMR, IR, and AC impedance spectroscopy characterization. *Chem. Mater.* **2011**, *23*, 3970-7. DOI
58. Buschmann, H.; Dölle, J.; Berendts, S.; et al. Structure and dynamics of the fast lithium ion conductor "$Li_7La_3Zr_2O_{12}$". *Phys. Chem. Chem. Phys.* **2011**, *13*, 19378-92. DOI
59. Kuhn, A.; Choi, J.; Robben, L.; Tietz, F.; Wilkening, M.; Heitjans, P. Li ion dynamics in Al-doped garnet-type $Li_7La_3Zr_2O_{12}$ crystallizing with cubic symmetry. *Z. für. Phys. Chem.* **2012**, *226*, 525-37. DOI
60. Düvel, A.; Kuhn, A.; Robben, L.; Wilkening, M.; Heitjans, P. Mechanosynthesis of solid electrolytes: preparation, characterization,

and Li ion transport properties of garnet-type Al-doped $Li_7La_3Zr_2O_{12}$ crystallizing with cubic symmetry. *J. Phys. Chem. C.* **2012**, *116*, 15192-202. DOI

61. Rettenwander, D.; Blaha, P.; Laskowski, R.; et al. DFT study of the role of Al^{3+} in the fast ion-conductor $Li_{7-3x}Al^{3+}_xLa_3Zr_2O_{12}$ garnet. *Chem. Mater.* **2014**, *26*, 2617-23. DOI PubMed PMC
62. Rettenwander, D.; Geiger, C. A.; Tribus, M.; Tropper, P.; Amthauer, G. A synthesis and crystal chemical study of the fast ion conductor $Li_{7-3x}Ga_xLa_3Zr_2O_{12}$ with x = 0.08 to 0.84. *Inorg. Chem.* **2014**, *53*, 6264-9. DOI PubMed PMC
63. Bernuy-lopez, C.; Manalastas, W.; Lopez, A. J. M.; Aguadero, A.; Aguesse, F.; Kilner, J. A. Atmosphere controlled processing of Ga-substituted garnets for high Li-ion conductivity ceramics. *Chem. Mater.* **2014**, *26*, 3610-7. DOI
64. Rettenwander, D.; Langer, J.; Schmidt, W.; et al. Site Occupation of Ga and Al in Stabilized Cubic $Li_{7-3(x+y)}Ga_xAl_yLa_3Zr_2O_{12}$ garnets as deduced from ^{27}Al and ^{71}Ga MAS NMR at ultrahigh magnetic fields. *Chem. Mater.* **2015**, *27*, 3135-42. DOI
65. Rettenwander, D.; Wagner, R.; Langer, J.; Maier, M. E.; Wilkening, M.; Amthauer, G. Crystal chemistry of "$Li_7La_3Zr_2O_{12}$" garnet doped with Al, Ga, and Fe: a short review on local structures as revealed by NMR and Mößbauer spectroscopy studies. *Eur. J. Mineral.* **2016**, *28*, 619-29. DOI
66. Karasulu, B.; Emge, S. P.; Groh, M. F.; Grey, C. P.; Morris, A. J. Al/Ga-doped $Li_7La_3Zr_2O_{12}$ garnets as Li-ion solid-state battery electrolytes: atomistic insights into local coordination environments and their influence on ^{17}O, ^{27}Al, and ^{71}Ga NMR Spectra. *J. Am. Chem. Soc.* **2020**, *142*, 3132-48. DOI PubMed PMC
67. Vema, S.; Berge, A. H.; Nagendran, S.; Grey, C. P. Clarifying the dopant local structure and effect on ionic conductivity in garnet solid-state electrolytes for lithium-ion batteries. *Chem. Mater.* **2023**, *35*, 9632-46. DOI PubMed PMC
68. Wang, D.; Zhong, G.; Pang, W. K.; et al. Toward understanding the lithium transport mechanism in garnet-type solid electrolytes: Li^+ ion exchanges and their mobility at octahedral/tetrahedral sites. *Chem. Mater.* **2015**, *27*, 6650-9. DOI
69. Ranque, P.; Zagórski, J.; Devaraj, S.; Aguesse, F.; López, A. J. M. Characterization of the interfacial Li-ion exchange process in a ceramic-polymer composite by solid state NMR. *J. Mater. Chem. A.* **2021**, *9*, 17812-20. DOI
70. Ghorbanzade, P.; Accardo, G.; Gomez, K.; et al. Influence of the LLZO-PEO interface on the micro- and macro-scale properties of composite polymer electrolytes for solid-state batteries. *Mater. Today. Energy.* **2023**, *38*, 101448. DOI
71. Ghorbanzade, P.; Pesce, A.; Gómez, K.; et al. Impact of thermal treatment on the Li-ion transport, interfacial properties, and composite preparation of LLZO garnets for solid-state electrolytes. *J. Mater. Chem. A.* **2023**, *11*, 11675-83. DOI
72. Zheng, J.; Tang, M.; Hu, Y. Lithium ion pathway within $Li_7La_3Zr_2O_{12}$-polyethylene oxide composite electrolytes. *Angewandte. Chemie.* **2016**, *128*, 12726-30. DOI
73. Hu, W.; Chien, P.; Wu, N.; Zhong, S. High Li^+ conducting porous garnet enables fast Li^+ conduction in polymer/garnet composite electrolyte. *ACS. Appl. Energy. Mater.* **2024**, *7*, 8077-84. DOI
74. Lu, Z.; Peng, L.; Rong, Y.; et al. Enhanced electrochemical properties and optimized Li^+ transmission pathways of PEO/LLZTO-based composite electrolytes modified by supramolecular combination. *Energy. Environ. Mater.* **2024**, *7*, e12498. DOI
75. Yang, T.; Zheng, J.; Cheng, Q.; Hu, Y. Y.; Chan, C. K. Composite polymer electrolytes with $Li_7La_3Zr_2O_{12}$ garnet-type nanowires as ceramic fillers: mechanism of conductivity enhancement and role of doping and morphology. *ACS. Appl. Mater. Interfaces.* **2017**, *9*, 21773-80. DOI
76. Zheng, J.; Dang, H.; Feng, X.; Chien, P.; Hu, Y. Li-ion transport in a representative ceramic-polymer-plasticizer composite electrolyte: $Li_7La_3Zr_2O_{12}$-polyethylene oxide-tetraethylene glycol dimethyl ether. *J. Mater. Chem. A.* **2017**, *5*, 18457-63. DOI
77. He, J.; Chen, H.; Wang, D.; Zhang, Q.; Zhong, G.; Peng, Z. Interfacial barrier of ion transport in poly (ethylene oxide)-$Li_7La_3Zr_2O_{12}$ composite electrolytes illustrated by ^6Li-tracer nuclear magnetic resonance spectroscopy. *J. Phys. Chem. Lett.* **2022**, *13*, 1500-5. DOI
78. Wu, L.; Wang, Y.; Tang, M.; et al. Lithium-ion transport enhancement with bridged ceramic-polymer interface. *Energy. Storage. Mater.* **2023**, *58*, 40-7. DOI
79. Zhang, X.; Cheng, S.; Fu, C.; et al. Unveiling the structure and diffusion kinetics at the composite electrolyte interface in solid-state batteries. *Adv. Energy. Mater.* **2024**, *14*, 2401802. DOI
80. Koch, B.; Vogel, M. Lithium ionic jump motion in the fast solid ion conductor $Li_5La_3Nb_2O_{12}$. *Solid. State. Nucl. Magn. Reson.* **2008**, *34*, 37-43. DOI PubMed
81. Narayanan, S.; Epp, V.; Wilkening, M.; Thangadurai, V. Macroscopic and microscopic Li^+ transport parameters in cubic garnet-type "$Li_{6.5}La_{2.5}Ba_{0.5}ZrTaO_{12}$" as probed by impedance spectroscopy and NMR. *RSC. Adv.* **2012**, *2*, 2553. DOI
82. Kuhn, A.; Narayanan, S.; Spencer, L.; Goward, G.; Thangadurai, V.; Wilkening, M. Li self-diffusion in garnet-type $Li_7La_3Zr_2O_{12}$ as probed directly by diffusion-induced ^7Li spin-lattice relaxation NMR spectroscopy. *Phys. Rev. B.* **2011**, 83. DOI
83. Bottke, P.; Rettenwander, D.; Schmidt, W.; Amthauer, G.; Wilkening, M. Ion Dynamics in solid electrolytes: NMR reveals the elementary steps of Li^+ hopping in the garnet $Li_{6.5}La_3Zr_{1.75}Mo_{0.25}O_{12}$. *Chem. Mater.* **2015**, *27*, 6571-82. DOI
84. Böhmer, R.; Jeffrey, K.; Vogel, M. Solid-state Li NMR with applications to the translational dynamics in ion conductors. *Prog. Nucl. Magn. Reson. Spectrosc.* **2007**, *50*, 87-174. DOI
85. Kuhn, A.; Epp, V.; Schmidt, G.; Narayanan, S.; Thangadurai, V.; Wilkening, M. Spin-alignment echo NMR: probing Li^+ hopping motion in the solid electrolyte $Li_7La_3Zr_2O_{12}$ with garnet-type tetragonal structure. *J. Phys. Condens. Matter.* **2012**, *24*, 035901. DOI PubMed
86. Hayamizu, K.; Matsuda, Y.; Matsui, M.; Imanishi, N. Lithium ion diffusion measurements on a garnet-type solid conductor $Li_{6.6}La_3Zr_{1.6}Ta_{0.4}O_{12}$ by using a pulsed-gradient spin-echo NMR method. *Solid. State. Nucl. Magn. Reson.* **2015**, *70*, 21-7. DOI PubMed

87. Hayamizu, K.; Seki, S.; Haishi, T. Lithium ion micrometer diffusion in a garnet-type cubic $Li_7La_3Zr_2O_{12}$ (LLZO) studied using ^{7}Li NMR spectroscopy. *J. Chem. Phys.* **2017**, *146*, 024701. DOI
88. Hayamizu, K.; Seki, S.; Haishi, T. Non-uniform lithium-ion migration on micrometre scale for garnet- and NASICON-type solid electrolytes studied by ^{7}Li PGSE-NMR diffusion spectroscopy. *Phys. Chem. Chem. Phys.* **2018**, *20*, 17615-23. DOI PubMed
89. Hayamizu, K.; Terada, Y.; Kataoka, K.; Akimoto, J.; Haishi, T. Relationship between Li^+ diffusion and ion conduction for single-crystal and powder garnet-type electrolytes studied by ^{7}Li PGSE NMR spectroscopy. *Phys. Chem. Chem. Phys.* **2019**, *21*, 23589-97. DOI PubMed
90. Hayamizu, K.; Terada, Y.; Kataoka, K.; Akimoto, J. Toward understanding the anomalous Li diffusion in inorganic solid electrolytes by studying a single-crystal garnet of LLZO-Ta by pulsed-gradient spin-echo nuclear magnetic resonance spectroscopy. *J. Chem. Phys.* **2019**, *150*, 194502. DOI PubMed
91. Kataoka, K.; Akimoto, J. High ionic conductor member of garnet-type oxide $Li_{6.5}La_3Zr_{1.5}Ta_{0.5}O_{12}$. *Chem. Electro. Chem.* **2018**, *5*, 2551-7. DOI
92. Kuhn, A.; Kunze, M.; Sreeraj, P.; et al. NMR relaxometry as a versatile tool to study Li ion dynamics in potential battery materials. *Solid. State. Nucl. Magn. Reson.* **2012**, *42*, 2-8. DOI
93. Castillo, A.; Charpentier, T.; Rapaud, O.; et al. Bulk Li mobility enhancement in Spark Plasma Sintered $Li_{7-3x}Al_xLa_3Zr_2O_{12}$ garnet. *Ceram. Int.* **2018**, *44*, 18844-50. DOI
94. Wagner, R.; Redhammer, G. J.; Rettenwander, D.; et al. Crystal structure of garnet-related Li-ion conductor Li_{7-3x} $Ga_xLa_3Zr_2O_{12}$: fast Li-ion conduction caused by a different cubic modification? *Chem. Mater.* **2016**, *28*, 1861-71. DOI
95. Hogrefe, K.; Minafra, N.; Zeier, W. G.; Wilkening, H. M. R. Tracking ions the direct way: long-range Li^+ dynamics in the thio-LISICON family Li_4MCh_4 (M = Sn, Ge; Ch = S, Se) as probed by ^{7}Li NMR relaxometry and ^{7}Li spin-alignment echo NMR. *J. Phys. Chem. C. Nanomater. Interfaces.* **2021**, *125*, 2306-17. DOI
96. Duff, B. B.; Elliott, S. J.; Gamon, J.; Daniels, L. M.; Rosseinsky, M. J.; Blanc, F. Toward understanding of the Li-Ion migration pathways in the lithium aluminum sulfides Li_3AlS_3 and $Li_{4.3}AlS_{3.3}Cl_{0.7}$ via ^{6,7}Li solid-state nuclear magnetic resonance spectroscopy. *Chem. Mater.* **2023**, *35*, 27-40. DOI
97. Ganapathy, S.; Yu, C.; van, E. E. R. H.; Wagemaker, M. Peeking across grain boundaries in a solid-state ionic conductor. *ACS. Energy. Lett.* **2019**, *4*, 1092-7. DOI
98. Han, F.; Westover, A. S.; Yue, J.; et al. High electronic conductivity as the origin of lithium dendrite formation within solid electrolytes. *Nat. Energy.* **2019**, *4*, 187-96. DOI
99. Tian, H.; Liu, Z.; Ji, Y.; Chen, L.; Qi, Y. Interfacial electronic properties dictate Li dendrite growth in solid electrolytes. *Chem. Mater.* **2019**, *31*, 7351-9. DOI
100. Shen, F.; Dixit, M. B.; Xiao, X.; Hatzell, K. B. Effect of pore connectivity on Li dendrite propagation within LLZO electrolytes observed with synchrotron X-ray tomography. *ACS. Energy. Lett.* **2018**, *3*, 1056-61. DOI
101. Marbella, L. E.; Zekoll, S.; Kasemchainan, J.; Emge, S. P.; Bruce, P. G.; Grey, C. P. ^{7}Li NMR chemical shift imaging to detect microstructural growth of lithium in all-solid-state batteries. *Chem. Mater.* **2019**, *31*, 2762-9. DOI PubMed PMC
102. Chandrashekar, S.; Trease, N. M.; Chang, H. J.; Du, L. S.; Grey, C. P.; Jerschow, A. ^{7}Li MRI of Li batteries reveals location of microstructural lithium. *Nat. Mater.* **2012**, *11*, 311-5. DOI PubMed
103. Chang, W.; May, R.; Wang, M.; et al. Evolving contact mechanics and microstructure formation dynamics of the lithium metal-$Li_7La_3Zr_2O_{12}$ interface. *Nat. Commun.* **2021**, *12*, 6369. DOI PubMed PMC
104. Pecher, O.; Carretero-González, J.; Griffith, K. J.; Grey, C. P. Materials' methods: NMR in battery research. *Chem. Mater.* **2017**, *29*, 213-42. DOI
105. Tang, M.; Sarou-Kanian, V.; Melin, P.; et al. Following lithiation fronts in paramagnetic electrodes with in situ magnetic resonance spectroscopic imaging. *Nat. Commun.* **2016**, *7*, 13284. DOI PubMed PMC
106. Nishiyama, Y.; Hou, G.; Agarwal, V.; Su, Y.; Ramamoorthy, A. Ultrafast magic angle spinning solid-state NMR spectroscopy: advances in methodology and applications. *Chem. Rev.* **2023**, *123*, 918-88. DOI PubMed PMC
107. Steinberg, Y.; Sebti, E.; Moroz, I. B.; et al. Composition and structure of the solid electrolyte interphase on Na-ion anodes revealed by exo- and endogenous dynamic nuclear polarization - NMR spectroscopy. *J. Am. Chem. Soc.* **2024**, *146*, 24476-92. DOI PubMed PMC
108. Maity, A.; Svirinovsky-Arbeli, A.; Buganim, Y.; Oppenheim, C.; Leskes, M. Tracking dendrites and solid electrolyte interphase formation with dynamic nuclear polarization-NMR spectroscopy. *Nat. Commun.* **2024**, *15*, 9956. DOI PubMed PMC
109. Hogrefe, K.; Stainer, F.; Minafra, N.; Zeier, W. G.; Wilkening, H. M. R. NMR down to cryogenic temperatures: accessing the rate-limiting step of Li transport in argyrodite electrolytes. *Chem. Mater.* **2024**, *36*, 6527-34. DOI
110. Chien, P. H.; Feng, X.; Tang, M.; et al. Li Distribution heterogeneity in solid electrolyte $Li_{10}GeP_2S_{12}$ upon electrochemical cycling probed by ^{7}Li MRI. *J. Phys. Chem. Lett.* **2018**, *9*, 1990-8. DOI